Elemental partitioning, mechanical and oxidation behaviour of two high-γ' W-free γ/γ' polycrystalline Co/Ni superalloys

Ioannis Bantounas[a,*], Bharat Gwalani[b], Talukder Alam[b], Rajarshi Banerjee[b], David Dye[a]

[a] *Department of Materials, Imperial College, South Kensington, London SW7 2AZ, UK*
[b] *Department of Materials Science and Engineering, University of North Texas, Denton, TX 76207, USA*

Abstract

Cr-containing W-free Co alloys that form $L1_2$ γ' strengthening precipitates in an fcc γ matrix are presented to examine the effect of Ta and Nb additions to increase the strength, solvus temperature and gamma prime fraction. The alloys are found to have relatively low density, good oxidation resistance (<0.5 µm scale at 800°C for 100 h) with coherent Al_2O_3 and Cr_2O_3 scales, and reasonable yield strengths, ∼800 MPa. The phase partitioning, measured by atom probe tomography, was found to be similar to W-containing Co/Ni superalloys, with Mo partitioning to the matrix providing solid solution strengthening.

Keywords: Cobalt-base superalloys, Tungsten, $L1_2$ compound, APT, Oxidation, γ-γ' microstructure, High temperature strength, Density

The precipitation of an ordered $L1_2$ phase in the Co-Al-W ternary system <1; 2> has enabled the development of Co-base alloys with increased high temperature strength <3–5>. Advantages of Co-Al-W alloys include a large processing window between the γ' solvus and the solidus temperature <6>, making them suitable as wrought alloys, as well as mechanical properties comparable to first generation Ni-base superalloys <7>. The high W content required to stabilise the γ' phase, however, unfavourably increases their density.

Makineni *et al.* <8–10> stabilised the γ' phase in the Co-Al-Mo ternary with small additions of either Ta or Nb, thus substituting W and acheiving a welcome reduction in density from 9.3–9.9 g/cm^3 to 8.36–8.65 g/cm^3. Nb containing Co-Al-Mo alloys have superior specific yield strengths compared to Co-Al-W alloys <8; 9>. Replacing Nb with Ta improves the room temperature and high temperature yield stress as well as the γ' solvus temperature <10>. The flow stress and γ' solvus temperatures can be further increased via Ni additions to the Co-Al-Mo-Ta/Nb alloys <8; 10> or Ti additions to Ta containing alloys <10>. Adding Cr to the Ni containing W-free alloys further improves the high temperature flow stress and γ' solvus temperature <11>. Though the specific strength of these W-free Co-Al-Mo γ/γ' alloys is promising, their oxidation resistance has yet to be explored.

In the current study, we examine the partitioning of elements, flow stress and oxidation resistance of two Co-Al-Mo γ/γ' alloys investigating the effects of Nb and Ta additions. Both alloys contained Cr for improved oxidation resistance and Ni to stabilise the γ'. The Ni and Cr contents were developed based on previous experience to provide oxidation resistance similar to that of polycrystalline Ni superalloys, whilst being cautious on the overall phase stability.

Two alloys with nominal compositions listed in Table 1 were melted in a vacuum arc-melter backfilled with argon and poured into a 23 × 23 × 60 mm mould. Alloy 2Ta1Nb was encapsulated in quartz and homogenised at 1200°C for 144 h while 3Ta0Nb was homogenised in a vacuum furnace at 1250°C for 48 h. The 3Ta0Nb ingot was profile rolled to a 13 × 13 mm cross section while 2Ta1Nb was cut lengthwise into quarters and flat rolled to a final thickness of 2.5 mm. The maximum strain per pass during rolling for 2Ta1Nb and 3Ta0Nb was 24% and 16%, respectively. Both alloys were subsequently solution treated at 1050 °C for 4 h, cooled at a rate of 0.3 °C/s to 900 °C and aged for 16 h, and finally cooled to 850 °C and aged for 4 h prior to furnace cooling to room temperature. The average grain size of alloys 2Ta1Nb and 3Ta0Nb was 34 and 52 µm, respectively, as measured from optical micrographs following the Abrams 3 circle method outlined in ASTM E112.32609.

The final microstructures are displayed in Fig. 1, acquired using a Zeiss Sigma 300 scanning electron microscope. X-ray energy-dispersive spectroscopy (XEDS) spot patterns were acquired using a JEOL 6400 scanning electron microscopy equipped with a INCA x-sight EDS detector from Oxford Instruments. Specimens for APT experi-

*Corresponding author
Email addresses: ioannis.bantounas@imperial.ac.uk (Ioannis Bantounas), bharatgwalani@my.unt.edu (Bharat Gwalani), talukder.alam@unt.edu (Talukder Alam), raj.banerjee@unt.edu (Rajarshi Banerjee), david.dye@imperial.ac.uk (David Dye)

ments were prepared by the standard lift-out method <12>, using an FEI Nova 200 NanoLab system equipped with a Gas Injection System (GIS) for Pt deposition and an Omniprobe micromanipulator for sample relocation. APT experiments were performed using a LEAP 3000X HR (Cameca Instruments, Inc.), operated in laser mode (0.5 nJ) at a stage temperature of 45K and a target evaporation of 0.5%. IVAS 3.8.10 software (Cameca) was used for data reconstruction and analysis.

Differential scanning calorimetry (DSC) was used to determine the γ' solvus temperature for each composition using a Mettler Toledo TGA/DSC 2 thermal analysis system. Specimens were cut to $2 \times 2 \times 3$ mm and heated to 1200°C. Heating/cooling rates were set to 10 °C/min with the γ' solvus temperature measured from the cooling cycle.

The oxidation performance was tested at 800 °C for 100 h in laboratory air. Specimen dimensions for this test were $3.5 \times 3.5 \times 6.0$ mm. Oxidation damage was assessed by measuring the external and internal oxide thickness, and the γ' dissolution zone. Measurements were taken from cross-sections of the oxidised surface prepared with a focussed ion beam (FIB) microscope. The oxide cross-sections displayed in Fig. 4 (a) and (b) were prepared on a Zeiss Auriga Cross-Beam and imaged with the InLens EsB (energy selective backscatter) detector. Due to the difficulty in determining the oxide thickness in 3Ta0Nb the values quoted in Table 1 were calculated by milling a ramp inclined at 30° to the oxide surface using a FEI FIB200-SIMS workstation. This exposed more of the oxide to the incident beam, t_{viewed}, reducing the error in the measurement, with the oxide thickness $t_{\text{true}} = t_{\text{viewed}} \tan(30°)$.

Transmission electron microscopy (TEM) lamellae were prepared from the oxidised specimens using an FEI Helios Nanolab 600 focussed ion beam workstation via the in situ lift-out technique <13; 14>. The oxide chemistry was examined in a JEOL JEM-2100F microscope equipped with a XEDS silicon-drift detector from Oxford Instruments. XEDS data was collected and analysed with the Oxford Instruments AZTec v3.1 software package.

Tensile properties were tested on dogbones with a 1.5×1.5 mm cross section and 19.0 mm gauge length. Tests were performed at RT and in 50°C increments between 650°C and 900°C, at a strain rate of $10^{-3}\,\text{s}^{-1}$ in vacuum using a EZ005 Zwick. The density of the alloys was measured using Archimedes' principle following ASTM B311-08 guidelines.

Fig. 1 shows the microstructure of alloys 2Ta1Nb and 3Ta0Nb after rolling and heat treatment. Both alloys have inter- and intragranular secondary phases. XEDS measurements revealed the presence of MC carbides (white) <15> with (Ta,Nb)C present in the 2Ta1Nb alloy and TaC in the 2Ta0Nb alloy. The alloys also contain the tetragonal close-packed μ $(Mo,Ta)_6(Co,Ni)_7$ phase (grey) <16> as well as the cubic B2 (Co,Ni)Al phase (black) <17>. Fig. 1(c) and (d) show the γ/γ' two-phase microstructure. The spherical morphology of the precipitates is indicative of a low γ/γ' lattice misfit. This is attributed to the addition of Cr which replaces the larger Mo atoms in the γ' phase, thus lowering the misfit between the two phases <11>. Both alloys show a population of fine γ' precipitates within the γ channels. However, fewer such precipitates are observed in the Nb-free alloy.

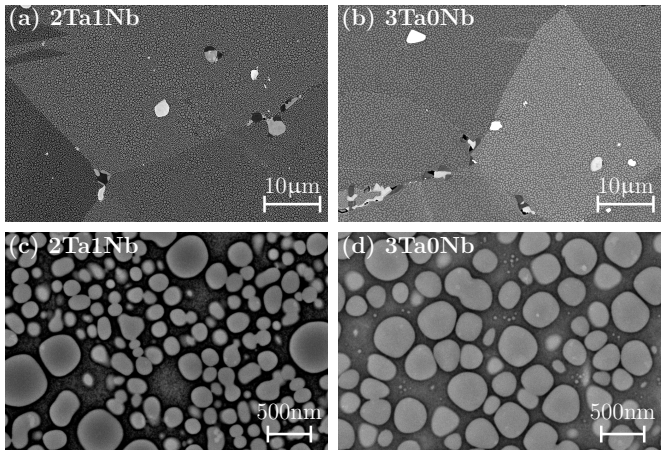

Figure 1: Backscattered-electron micrographs of grain boundary phases following hot rolling and heat treatment of alloys (a) 2Ta1Nb and (b) 3Ta0Nb, (c) and (d) reveal morphology of γ' phase.

Atom maps and proximity histograms generated from the two alloys are displayed in Fig. 2. Two generations of γ' precipitates are evident in both alloys from the atom maps, corroborating the observations from the electron micrographs. The compositional measurements for the matrix γ and precipitate γ' phases are given in Table 2. The elemental partitioning coefficient, k_i, is defined as the ratio of the concentration of an element, i, in the γ' phase to that in the γ phase, $k_i = C_{\gamma'}/C_{\gamma}$.

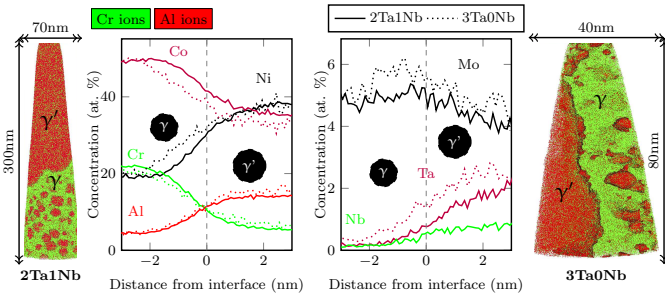

Figure 2: Atom maps of alloys 2Ta1Nb and 3Ta0Nb, using 10 and 8 at.% Al iso-concentration surface to distinguish γ-γ' interfaces, respectively, and proximity histograms of major (left) and minor (right) species across matrix and γ' interface. For clarity, only Al (red) and Cr (green) atoms are shown in the atom maps.

Co, Mo and Cr were all observed to partition to the γ matrix, $k_i < 1$. Co-Al-W superalloys with substantial Ni additions generally show Co partitioning to the γ phase <18–21>, but do so more strongly as the Ni content is increased, as observed in Ni superalloys <22>. The partitioning coefficients for Co observed here (0.65-0.67) are

Table 1: Measured composition (ICP-OES, Incotest, Hereford, UK) of alloys 2Ta1Nb and 3Ta0Nb, in at. %, together with oxidation, physical, and mechanical data.

Alloy	Measured Composition (at.%)										Oxidation (nm)				Density (gcm^{-3})	γ' solvus (°C)	Yield Stress (MPa)	
	Co	Ni	Cr	Al	Mo	Ta	Nb	C	B	Zr	External Oxide	Internal Oxide	γ' dissolution	Tot. Damage			RT	750°C
2Ta1Nb	40.26	31.07	10.67	10.60	3.99	**1.88**	**0.99**	0.31	0.19	0.04	327†	n/a†	711	1,038	8.23	1065	822	752
3Ta0Nb	40.18	31.14	10.87	10.76	4.03	**2.54**	–	0.22	0.22	0.05	290	216	1,467	1,757	8.47	1082	785	702

† The internal and external oxides have been measured together in A-2Ta1Nb. Their total depth has been recorded in the "External oxide" field.

Table 2: APT-measured compositions (and uncertainties σ) of the secondary γ'_s and of the matrix, in at.%, together with inferred partition coefficients $k = C_{\gamma'}/C_{\gamma}$ (2 s.f.).

Ion type	Alloy 2Ta1Nb Matrix at. %	σ %	γ' at. %	σ %	k_i	Alloy 3Ta0Nb Matrix at. %	σ %	γ' at. %	σ %	k_i
Cr	20.6	0.42	4.9	0.19	0.24	21.2	0.41	5.3	0.22	0.25
Mo	5.0	0.19	2.7	0.14	0.55	6.5	0.22	3.1	0.16	0.48
Co	51.2	0.74	34.2	0.57	0.67	50.5	0.71	32.8	0.61	0.65
Ni	18.1	0.39	39.6	0.63	2.2	16.1	0.35	38.3	0.67	2.4
Al	4.8	0.19	14.5	0.34	3.0	5.4	0.19	17.0	0.41	3.2
Ta	0.2	0.04	3.2	0.15	18	0.3	0.05	3.5	0.17	10
Nb	0.2	0.04	1.0	0.08	4.8	–	–	–	–	–

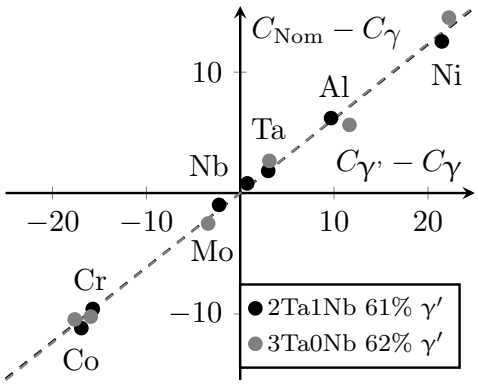

Figure 3: Volume fraction of γ' as measured from APT data using the lever rule.

similar to those reported by Makineni in alloys near 53Co-30Ni-10Al-5Mo-2Ta, 0.53-0.74 <10; 11>.

Cr favours the γ phase with similar partitioning coefficients, $k_{\text{Cr}} \sim 0.25$, for alloys 2Ta1Nb and 3Ta0Nb. Cr is generally found to partition to the γ in γ' forming Ni and Co superalloys. In Ni superalloys, k_{Cr} ranges between 0.08-0.31, dependent on Co:Ni ratio <22>. Adding Ni in Co-Ni-Al-W superalloys tended to decrease k_{Cr}, to 0.35 for Co:Ni = 3:2 <19> and further to 0.19 for Co:Ni = 1:1 <18>. In general, the more Ni rich the γ' precipitates the stronger Cr partitions to the γ matrix.

In contrast, Cr additions do not affect k_{Cr}. For example, in the Co-9Al-9W (at%) ternary alloy k_{Cr} remains $\sim$ 0.57 when doubling the Cr content from 4 to 8 at% <20>. This may aid in explaining the similarities in $k_{\text{Cr}} \sim 0.24$ between this work and that of Nithin *et al.* <11> despite the differences in Cr content, 13 vs 10 at.% respectively.

Mo partitions to the γ matrix with $k_{\text{Mo}} = 0.48$ and 0.55 in 2Ta1Nb and 3Ta0Nb, respectively. Interestingly, Mo partitions to the γ' phase, k_{Mo}=1.26, in Co-9Al-10W <23>. The preference for the γ phase is an effect of Cr, e.g. k_{Mo}=0.53 in Cr-containg Co-Ni-Al-W-Mo-Ta <19> and 0.78-0.87 in Co-Ni-Al-Mo-Ta (W-free) alloys <11>. Ab-initio simulations show this to be due to Cr replacing Mo in the γ' <11>. Additionally, the Mo excess observed at γ/γ' interfaces <11; 21> is suppressed by Cr additions <11; 21>.

It is interesting to note the higher values of k_{Mo} reported by Nithin *et al.* <11> on Cr containing Co-Ni-Al-Mo alloys, 0.78-0.87, compared to the current study, 0.48-0.55, despite the similar bulk compositions of alloys 10Cr2Ta <11> and 3Ta0Nb. This will be discussed in more detail later on.

The second majority element, Ni, along with additions of Al, Ta and Nb partition to the ordered γ' phase, $k_i > 1$. Values of k_{Ni} reported in the present work are a little higher (2.2 and 2.4) than those found in the literature (1.0–2.3) <11; 18; 21; 22>. Al partitions strongly to the γ' in the present study. The current alloys have values of 3.0 and 3.2, this is within the upper band of the reported k_{Al} range for Co-base superalloys, 1.0 to 3.5 <10; 11; 18–21; 23; 24>.

Ta is added to Co-Al-W based superalloys as a γ' strengthener. Partitioning coefficients k_{Ta} range between 1.1 and 26 <10; 11; 18; 19; 21; 23; 24>. Co-Al-W ternary

alloys with additions of 2 at.% Ta have partitioning coefficients between 5.3 and 5.5 <23; 24>. Additions of Ni do not show a drastic shift to this range, with values between 4.9 and 5.4 for concentrations of 30 and 10 at.% Ni, respectively <21>. Cr additions to Co-Al-W alloys with 30 at.% Ni lower k_{Ta} by only a small fraction to 4.4 <19>. Alterations to the Cr concentration of 6 and 10 at.% do not affect the aforementioned Ta partitioning <19>.

Given the similar composition between alloy 3Ta0Nb and that of 10Cr2Ta by Nithin *et al.* <11> a comparison between the reported partitioning coefficients is worthwhile. Both alloys have comparable Co and Cr partitioning coefficients. Ni, Al, and Ta, however, are found to partition more heavily to the γ' phase in the present study. Additionally, Mo partitions more strongly to the matrix in 3Ta0Nb compared to 10Cr2Ta <11>. The similar bulk alloy composition between alloys 10Cr2Ta <11> and 3Ta0Nb make it difficult to account for the difference in partitioning based on composition alone.

However, an explanation may lie in the different heat treatments employed between the two studies. The current alloys were aged for 16 h at 900°C, while those in ref. <11> were aged for 50 h allowing more time for the phases to reach thermodynamic equilibrium. It should also be noted that no additional phases have been reported in the 10Cr2Ta alloy <11>. This is in contrast to the current set of alloys were additions of C, B and Zr result in MC carbides which may be responsible for the $(\mathrm{Mo,Ta})_6(\mathrm{Co,Ni})_7$ μ and (Co,Ni)Al B2 phases observed.

From the lever rule, the alloy (C^i_{Nom}) and phase compositions ($C^i_{\gamma'}$ and C^i_{γ}) can be used to estimate the γ' fractions, $V_{\gamma'}$. Where $V_{\gamma'} = (C^i_{\mathrm{Nom}} - C^i_{\gamma})/(C^i_{\gamma'} - C^i_{\gamma})$ for the element i. The data for alloying elements are shown in Fig. 3, indicating that γ' fractions of $> 60\%$ were obtained.

The γ' solvus temperatures of 2Ta1Nb and 3Ta0Nb were 1065°C and 1082°C, respectively, Table 1. The addition of 1 at.% Ta in place of Nb increases the γ' solvus temperature by more than 15°C. These values are comparable with published literature on Cr containing Co-Ni-Al-Mo-Ta alloys, e.g. 1038°C for 10Cr2Ta and 1078°C for 10Cr2Ta2Ti <11>. The density of the two alloys is 8.23 and 8.47 g/cm^3, Table 1. The lower density of 2Ta1Nb can be attributed to the replacement of 1 at.% Ta with Nb.

Oxidation performance was measured after exposing the alloys to air at 800°C for 100 h. Measurements of the internal oxide, external oxide and γ' depletion zone thickness from oxide cross-sections are reported in Table 1. The oxidation resistance of the current alloys show improvement over commercial Ni-base superalloys, e.g. oxide thickness of RR1000 after 100 h at 800°C is ∼1.75 μm <25> compared to ∼500 nm for 3Ta0Nb. Nb additions are found to improve the oxidation performance. The total damage depth of 2Ta1Nb and 3Ta0Nb is 1.0 and 1.8 μm, respectively. This is in agreement with the work of Weng *et al.* <26> on a Ni-20Cr based alloy, however, contrasts the findings of Klein *et al.* <27> who found Nb to worsen oxi-

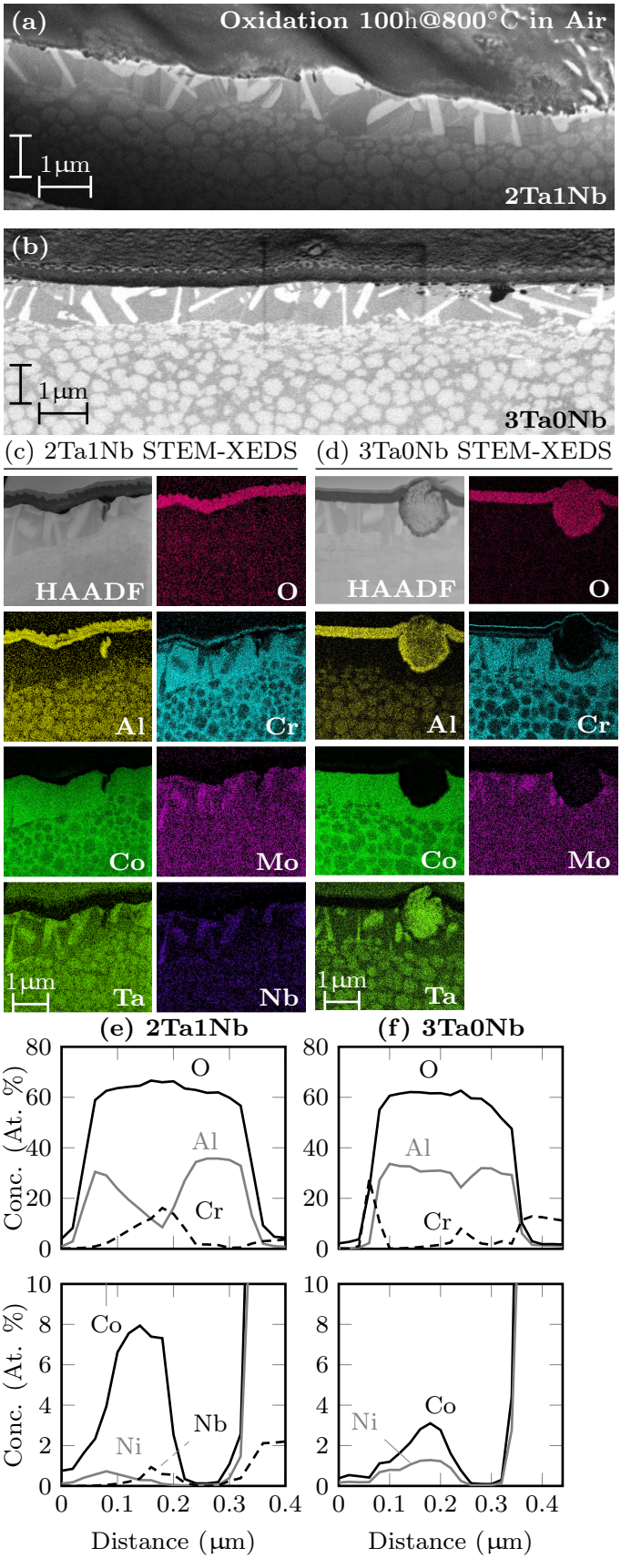

Figure 4: InLens EsB micrographs of FIB cross-section showing oxidation damage after 800°C for 100 h in air for alloys 2Ta1Nb (a) and 3Ta0Nb (b). (c) and (d) HAADF micrograph and elemental maps of TEM foils prepared from the oxidised surface of 2Ta1Nb and 3Ta0Nb, respectively. (e) and (f) XEDS linescans across the oxides (oxide/oxygen interface on the left and oxide/alloy interface on the right of the graphs).

dation properties in Co-9Al-8W-2Ta. It is speculated that this difference in the effect of Nb on the oxidation performance is related to Cr content, further work is being pursued to elucidate the effect of Nb on oxidation.

High-angle annular dark field (HAADF) scanning (S)TEM micrographs and XEDS elemental maps of the oxidised alloys are shown in Fig. 4 (c) and (d) for 2Ta1Nb and 3Ta0Nb, respectively. The elemental maps reveal a coherent aluminium rich oxide on the surface of both alloys with a Cr enriched layer in the middle. Beneath the oxide a γ' depleted zone is evident. This region consists of Ta/Mo enriched platelets within a recrystallised γ phase. Based on their morphology and composition, the platelets are likely to be the orthorhombic DOa $(Co,Ni)_3(Ta,Mo,Nb)$ δ phase <28>. The oxide of alloy 3Ta0Nb included an oxidised Ta carbide residing on the surface of the specimen, evident on the top right of the elemental maps in Fig. 4 (d).

Linescans across the oxide of alloys 2Ta1Nb and 3Ta0Nb are shown in Fig. 4 (e) and (f), respectively. The oxide of alloy 2Ta1Nb is enriched in aluminium at the oxide/oxygen interface. Beneath this initial Al rich layer there is an increase in Ni and Co concentration, followed by Cr in the centre of the oxide. The remaining oxide being predominantly Al rich at the oxide/alloy interface. Selected area diffraction patterns (SADPs) from the oxide contain Al_2O_3 and Cr_2O_3 spots, Fig. 5, suggesting the Al rich layers to be alumina and that Cr is present as chromia in the oxide and is not in solution with the alumina. Nb can be observed to reside within the Cr enriched region of the oxide and we presume it to be in solution with the Cr_2O_3. A similar trend is followed for the 3Ta0Nb alloy, however, a layer of chromia occupies the oxide/oxygen interface in this alloy instead of alumina, Fig. 4 (f). The stoichiometry of the oxide in both alloys is oxygen rich, suggesting the presence of cation vacancies.

The temperature dependence on 0.5% flow stress for tests conducted in tension under vacuum is shown in Fig. 6 (c), with the engineering stress-strain curves for the room tempertature (RT) and 800°C test shown in Fig. 6 (d). The RT hardening rate of both alloys is similar to that of modern Ni-base superalloys. The Nb containing alloy is stronger up to 800°C. Investigating the microstrucutre after a 1 h hold at 800°C and subsequently ice water quenching revealed that the fine γ' within the γ channels were present at this temperature. Above 800°C alloy 3Ta0Nb has a better strength retention, with the largest difference of 70 MPa displayed at 900°C. Both alloys exhibit the anomalous increase in yield stress with temperature with peak flow stress values of approximately 750 MPa and 730 MPa for 2Ta1Nb and 3Ta0Nb, respectively. However, the peak flow stress for the Nb containing alloy occurs at a higher temperature, 750 °C vs 700 °C.

The 3Ta0Nb alloy outperforms the 10Cr2Ta alloy from ref. <11> up to a temperature of 800°C, above which both alloys show a similar response in flow stress. Provided the likeness in composition between the two alloys this is ex-

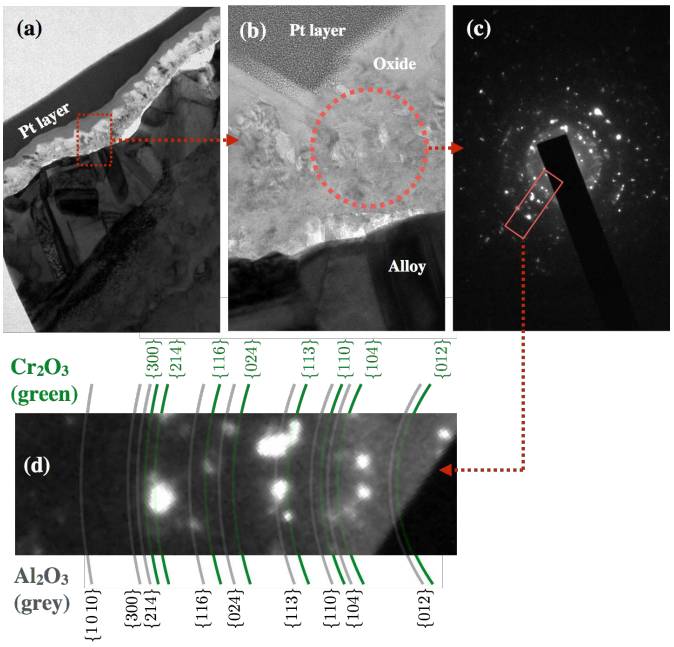

Figure 5: (a) and (b) Bright field TEM micrograph of oxide in alloy 2Ta1Nb after exposure to air at 800°C for 100 h. (c) and (d) SADP of oxide highlighting Al_2O_3 and Cr_2O_3 diffraction spots.

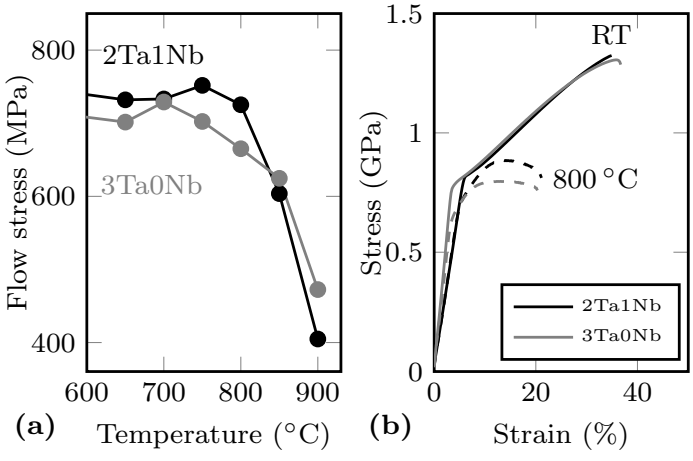

Figure 6: (a) Temperature dependence on tensile 0.5% flow stress, and (b) engineering tensile stress-strain curves tested at room temperature (RT) and 800°C.

plained by the different γ' distributions as a result of their ageing history. 10Cr2Ta <11> has been aged at 900°C for 50 h and is reported to have a unimodal γ' distribution with precipitates between 250-300 nm in size. The two-step ageing treatment in the current study has resulted in a multi-modal γ' distribution with coarse ∼380 nm precipitates and finer 10-30 nm within the γ channels. This has afforded a strength increase up to 800°C, above which the difference in flow stress between the two alloys diminishes, likely due to the dissolution of the finer γ' in the 3Ta0Nb alloy.

Compared to contemporary Ni-base alloys, such as ME3 <29> and RR1000 <25>, and Ni-Co-Al-W alloys <30>, the alloys examined here show improved oxidation resistance[1] and around 3.5% lower density. Their yield strength is rather low, being >1100 MPa in production alloys, over 25% higher. However, the alloys presented here have not been subject to extensive optimisation studies of the carbide and boride distributions, grain size refinement via powder processing or γ' size distribution, which together may provide such strength improvement. Therefore it may be attractive to examine the long term phase stability, creep and environmentally-assisted fatigue performance of alloys of this class in order to establish whether such optimisation efforts are justified.

In summary, W-free γ/γ' Co-Al-Mo superalloys have been developed with high Cr additions and the effect of Nb examined. Atom probe tomography studies show that Co, Mo and Cr partition to the γ matrix (k_{Co} = 0.65-0.67, k_{Mo} = 0.48-0.55 and k_{Cr} = 0.24-0.25) while Ni and Al segregate to the γ' phase (k_{Ni} = 2.2-2.4 and k_{Al} = 3.0-3.2). Ta and Nb partition strongly to the γ' (k_{Ta} = 10-18 and k_{Nb} = 4.8). The Nb containing alloy exhibits the stronger Ta partitioning of k_{Ta} = 18. Nb lowers the γ' solvus while improving the oxidation resistance at 800°C. Continuous chromia and alumina scales are observed after exposure to air at 800°C for 100 h. Both alloys show the anomalous flow stress effect with temperature, however, the Nb containing alloy displays peak flow stress at a higher temperature and is stronger at temperatures below 850°C.

The authors would like to thank Dr. Richard Chater for helpful advice on analysing oxidation damage using a FIB workstation and Dr. Stella Pedrazzini for helpful discussions regarding the STEM-XEDS data. This work was funded under the Rolls Royce–EPSRC strategic partnership in structural metallic systems for gas turbines (EP/M005607/1).

References

[1] C.S. Lee. Ph.D. thesis doctoral, The University of Arizona, 1971.

[2] J. Sato, T. Omori, K. Oikawa, I. Ohnuma, R. Kainuma, and K. Ishida. *Science*, 312:90–91, 2006.

[3] A. Suzuki and T.M. Pollock. *Acta Mater.*, 56(6):1288–1297, 2008.

[4] T.M. Pollock, J. Dibbern, M. Tsunekane, J. Zhu, and A. Suzuki. *JOM*, 62(1):58–63, 2010.

[5] A. Suzuki, H. Inui, and T.M. Pollock. *Annu. Rev. Mater. Res.*, 45:345–368, 2015.

[6] A. Bauer, S. Neumeier, F. Pyczak, and M. Goeken. *Scripta Mater.*, 63(12):1197–1200, 2010.

[7] S. Neumeier, L.P. Freund, and M. Göken. *Scripta Mater.*, 109:104–107, 2015.

[8] S.K. Makineni, B. Nithin, and K. Chattopadhyay. *Acta Mater.*, 85:85–94, 2015.

[9] S.K. Makineni, B. Nithin, and K. Chattopadhyay. *Scripta Mater.*, 98:36–39, 2015.

[10] S.K. Makineni, A. Samanta, T. Rojhirunsakool, T. Alam, B. Nithin, A.K. Singh, R. Banerjee, and K. Chattopadhyay. *Acta Mater.*, 97:29–40, 2015.

[11] B. Nithin, A. Samanta, S.K. Makineni, T. Alam, P. Pandey, A.K. Singh, R. Banerjee, and K. Chattopadhyay. *J. of Mater. Sci.*, 52(18):11036–11047, 2017.

[12] P.J. Felfer, T. Alam, S.P. Ringer, and J. Marie Cairney. *Microsc. Res. Tech.*, 75(4):484–491, 2012.

[13] L.A. Giannuzzi and F.A. Stevie. *Micron*, 30(3):197–204, 1999.

[14] J. Mayer, L.A. Giannuzzi, T. Kamino, and J. Michael. *MRS Bulletin*, 32:400–407, 2007.

[15] R.C. Reed. *The Superalloys: Fundamentals and Applications*. Cambridge University Press, 2006.

[16] K.P. Gupta. *J. Phase Equilib.*, 24(2):186–189, 2003.

[17] V. Raghavan. *J. Phase Equilib. Diff.*, 27(4):372–380, 2006.

[18] M. Knop, P. Mulvey, F. Ismail, A. Radecka, K.M. Rahman, T.C. Lindley, B.A. Shollock, M.C. Hardy, M.P. Moody, T.L. Martin, P.A.J. Bagot, and D. Dye. *JOM*, 66:2495–2501, 2014.

[19] S. Meher, L.J. Carroll, T.M. Pollock, and M.C. Carroll. *Scripta Mater.*, 113:185–189, 2016.

[20] I. Povstugar, C.H. Zenk, R. Li, P.-P. Choi, S. Neumeier, O. Dolotko, M. Hoelzel, M. Göken, and D. Raabe. *Mater. Sci. Tech.*, 32(3):220–225, 2016.

[21] E.A. Lass, D.J. Sauza, D.C. Dunand, and D.N. Seidman. *Acta Mater.*, 147:284–295, 2018.

[22] S.C.H. Llewelyn, K.A. Christofidou, V.J. Araullo-Peters, N.G. Jones, M.C. Hardy, E.A. Marquis, and H.J. Stone. *Acta Mater.*, 131:296 – 304, 2017.

[23] S. Meher and R. Banerjee. *Intermetallics*, 49:138–142, 2014.

[24] I. Povstugar, P.-P. Choi, S. Neumeier, A. Bauer, C.H. Zenk, M. Goeken, and D. Raabe. *Acta Mater.*, 78:78–85, 2014.

[25] A. Encinas-Oropesa, N.J. Simms, J.R. Nicholls, G.L. Drew, J. Leggett, and M.C. Hardy. *Mater. High Temp.*, 26(3):241–249, 2009.

[26] F. Weng, H. Yu, C. Chen, and K. Wan. *Mater. Manuf. Process.*, 30(11):1364–1369, 2015.

[27] L. Klein, A. Bauer, S. Neumeier, M. Goeken, and S. Virtanen. *Corrosion Sci.*, 53(5):2027–2034, 2011.

[28] Madeleine Durand-Charre. *The microstructure of superalloys*. Gordon and Breach, Amsterdam, 1997.

[29] C.K. Sudbrack, S.L. Draper, T.T. Gorman, J. Telesman, T. Gabb, and D.R. Hull. *Superalloys* (2012), 863–872 (TMS2012)

[30] F.B. Ismail, V.A. Vorontsov, T.C. Lindley, M.C. Hardy, D. Dye, and B.A. Shollock. *Corros. Sci.*, 116:44–52, 2017.

[1] Oxidation damage compared with tests conducted on alloy 3Ta0Nb at 800°C for 200 h, external oxide 478 nm, internal oxide 371 nm and γ' dissolution depth of 1,654 nm.